

Journal of Materials Chemistry B

Accepted Manuscript



This is an *Accepted Manuscript*, which has been through the Royal Society of Chemistry peer review process and has been accepted for publication.

Accepted Manuscripts are published online shortly after acceptance, before technical editing, formatting and proof reading. Using this free service, authors can make their results available to the community, in citable form, before we publish the edited article. We will replace this *Accepted Manuscript* with the edited and formatted *Advance Article* as soon as it is available.

You can find more information about *Accepted Manuscripts* in the [Information for Authors](#).

Please note that technical editing may introduce minor changes to the text and/or graphics, which may alter content. The journal's standard [Terms & Conditions](#) and the [Ethical guidelines](#) still apply. In no event shall the Royal Society of Chemistry be held responsible for any errors or omissions in this *Accepted Manuscript* or any consequences arising from the use of any information it contains.



Journal Name

Paper

Synthesis of Silica Nanoparticles with Controllable Surface Roughness for Therapeutic Protein Delivery

Yuting Niu,^a Meihua Yu,^a Jun Zhang,^a Yannan Yang,^a Chun Xu,^a Michael Yeh,^a Elena Taran,^b Jeff Jia Cheng Hou,^a Peter P Gray^a and Chengzhong Yu^{*a}

Received 00th January 20xx,
Accepted 00th January 20xx

DOI: 10.1039/x0xx00000x

www.rsc.org/

There is an increasing demand of efficient nano-carriers for intracellular delivery of therapeutic proteins. This study reports on a novel "neck-enhancing" approach to synthesize stable rough silica nanoparticles (RSNs) with controllable surface roughness. By increasing shell particle size from 13 to 98 nm while fixing core size (211 nm), the interspace size between neighboring shell particles of RSNs is enlarged from 7 to 38 nm. Cytochrome *c*, IgG fragment and IgG antibody is preferably absorbed onto one of the RSNs with the interspace size of 14, 21 and 38 nm, respectively. The binding activity of IgG fragment loaded in RSNs is maintained as confirmed by surface plasmon resonance. The hydrophobically modified RSNs with an interspace size of 38 nm effectively deliver therapeutic anti-pAkt antibody into breast cancer cells, causing a significant cell inhibition by blocking pAkt and the downstream anti-apoptotic protein of Bcl-2.

Introduction

Protein therapeutics has attracted increasing attention in cancer therapy due to the high specificity and less interference with normal biological processes.¹ By introducing proteins that specifically recognize and influence target molecules, deactivation or activation of key signalling pathways within cells can be manipulated, which strongly affect cell functions.² However, proteins are poorly delivered into cells owing to poor stability and inability to cross cell membranes.³ It remains an on-going challenge to develop delivery systems to efficiently compact and deliver therapeutic proteins for enhanced cancer therapy.⁴

In the past decade, various nano-carriers have been generated to deliver therapeutic proteins into cells, including liposomes,⁵⁻⁷ polymers,⁸⁻¹¹ inorganic nanoparticles¹²⁻¹⁴ and protein-based carriers.¹⁵ Among them, silica-based nanomaterials are a promising delivery platform for protein therapeutics. Bale et al.¹⁶ reported a successful delivery of the antibody to phospho-Akt (anti-pAkt) into MCF-7 cells with a significant cell inhibition where anti-pAkt antibody was absorbed on the surface of solid silica nanoparticles modified by n-octadecyltrimethoxy silane (n-ODMS). A recent study has demonstrated that there was an optimized pore size in the shell of silica hollow spheres for high

loading and improved intracellular delivery of a therapeutic protein, Ribonuclease A.¹⁷ The size of protein molecules may vary from several nanometres (e.g. cytochrome *c*¹⁸) to dozens of nanometres (e.g. IgG antibodies¹⁹). Therefore, it is highly desired to fabricate silica nanoparticles with adjustable voids to optimize the loading/release ability toward therapeutic proteins having various sizes.

Besides the interaction with cargo molecules, efficient cellular uptake performance of silica nanoparticles is a prerequisite factor for successful cellular delivery. Recently, silica nanoparticles mimicking the surface topography of enveloped viruses²⁰ were prepared by attaching shell particles with a smaller size onto core particles with a larger size.²¹ The interspaces between neighbouring shell particles provide the void space for the entrapment of biomolecules (e.g. siRNA). Compared to nanoparticles with smooth surfaces, silica nanoparticles with rough surfaces exhibited higher loading, sustained release and enhanced cellular uptake performance, consequently delivering siRNA successfully into cells. However, systematic control over core-to-shell size ratios of silica nanoparticles and their protein delivery efficacy has not been reported. If the surface roughness is adjustable on a nanoparticle, nano-carriers with advantages of both rough surface and controllable void space would be crucial for exploring the impact of interspace size on protein delivery efficiency. For silica nano-carriers with rough surface, it is also important to investigate the bioactivity of proteins, for example, the binding activity of antibody, after loading into void space. Answers to these questions will provide fundamental knowledge to the rational design of silica nano-carriers for therapeutic protein delivery.

Various approaches have been developed to fabricate rough nanoparticles by attaching small shell particles on a large core,

^a Australian Institute for Bioengineering and Nanotechnology, The University of Queensland, Brisbane, QLD 4067, Australia.

E-mail: c.yu@uq.edu.au; Fax: +61-7-334 63973; Tel: +61-7-334 63283

^b Australian National Fabrication Facility-QLD Node, Australian Institute for Bioengineering and Nanotechnology, The University of Queensland, Brisbane, QLD 4067, Australia.

† Electronic Supplementary Information (ESI) available: supporting Figures and Tables. See DOI: 10.1039/x0xx00000x

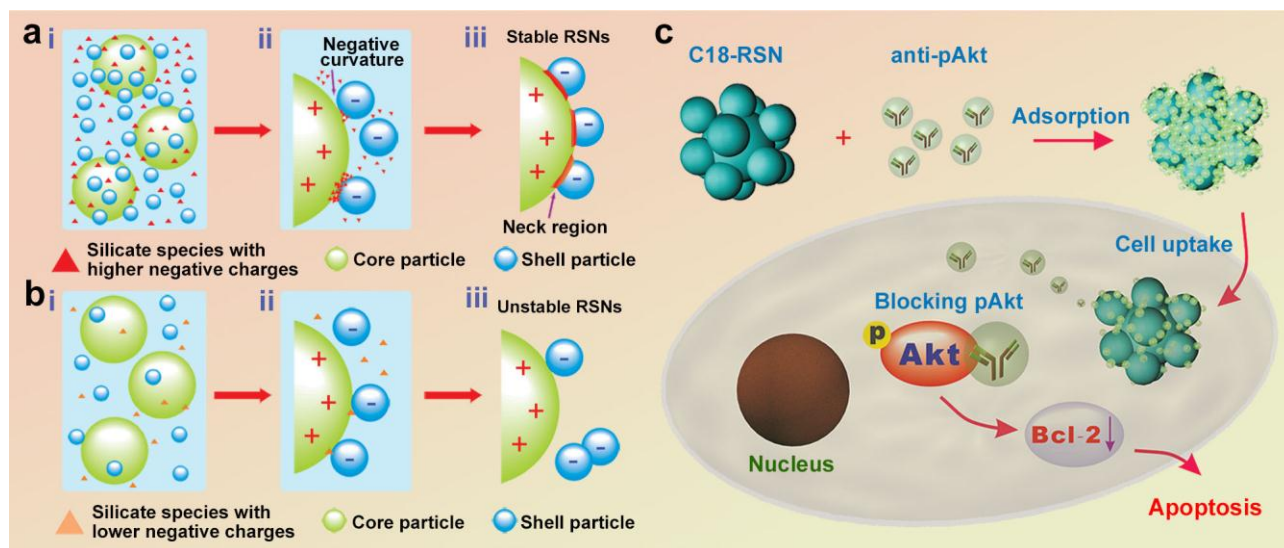


Fig. 1 Schematic illustrations of the synthesis of RSNs using a "neck-enhancing" approach (a) and a conventional interaction approach (b). Scheme c shows the cellular delivery of therapeutic anti-pAkt antibody using C18-RSNs and the cell inhibition mechanism.

including the electrostatic interaction^{22, 23} and covalent bonding pathways.²⁴ However, the synthesis of inorganic and/or organic rough nanoparticles with uniform sizes generally have larger particle sizes (> 400 nm), which is not ideal for cellular delivery.^{25, 26} Although rough nanoparticles with particle size of < 300 nm can be synthesized,²⁷⁻²⁹ the surface morphologies are not uniform. More importantly, in all previous literatures, the core-to-shell size ratio is larger than 5.6:1. Therefore, it is a challenge to attach shell particles with relatively large sizes onto core particles.

Herein we report a novel "neck-enhancing" approach to synthesize silica nanoparticles with controlled surface roughness. By roughening the surface of solid silica core particles (211 nm in diameter) with smaller shell particles (Fig. 1a) having various sizes, a series of rough silica nanoparticles (RSNs) are obtained. By forming a big "neck", shell particles with large sizes can be stably connected to the core particles. The surface roughness is correlated to the core-to-shell size ratios (from 16.2:1 to 2.2:1), and the interspace size between neighbouring shell particles increases from ~7 to ~38 nm with increasing shell particle sizes from ~13 to ~98 nm. The protein loading capacity of RSNs is dependent on the protein size relative to the interspace size. The optimal interspace size of RSNs for high protein loading capacity is ~7, ~21 and ~38 nm for cytochrome *c* (M.W. 12 kDa), IgG-fragment (IgG-F, domain antibody, M.W.76 kDa) and non-specific rabbit IgG antibody (IgG-A, M.W. 150 kDa), respectively. Using surface plasmon resonance (SPR), it is demonstrated that the IgG-F maintains efficient binding function after loading on RSNs. As shown in Fig. 1c, after hydrophobic modification of octadecyl-groups (C18), the C18-RSN with the interspace size of ~38 nm shows effective intracellular delivery of anti-pAkt antibody (having a similar structure and animal source with non-specific rabbit IgG-A) in human breast cancer (MCF-7) cells, leading to

significant cell inhibition by blocking pAkt and the downstream anti-apoptotic protein of Bcl-2.

Experimental

Materials and reagents

Ammonium hydroxide solution (28%), L-arginine, octane (98%), 3-aminopropyltriethoxysilane (APTES), cytochrome *c* (95%, from bovine heart), fetal bovine serum (FBS) and trypan blue solution (0.4%) were purchased from Sigma-Aldrich. Tetraethyl orthosilicate (TEOS, 98%) and n-octadecyltrimethoxy silane (n-ODMS, 90%) were purchased from Aldrich. Toluene was purchase from Merck. Dulbecco's Modified Eagle Medium (DMEM), penicillin-streptomycin (10000 U ml⁻¹) and trypsin-EDTA (0.25%) were purchased from GIBCO or Invitrogen, Life Sciences, Life Technologies. The monoclonal antibodies (rabbit source) to Bcl-2 and GAPDH and HRP-linked anti-rabbit IgG antibody were purchased from Cell Signalling. MCF-7 (HTB-22™) cell line was purchased from American Type Culture Collection (ATCC). IgG-F for adsorption and SPR measurement was kindly provided from Peter P Gray's group. All chemicals were used without further purifications.

Synthesis of core particle

Uniform nonporous silica core particles were synthesized using a well-known method developed by Stöber et al.³⁰ Typically, absolute ethanol (50 ml) was mixed with deionized (DI) water (3.8 ml) and ammonium hydroxide solution (2 ml) at 25 °C. Then, TEOS (3 ml) was added to the solution under vigorous stirring. After 6 h, the as-synthesized nanoparticles were separated by centrifugation at 20000 rpm, and washed with ethanol. The final product was obtained by drying at 100 °C overnight. After that, amine-silane was grafted to create

positively charged surface. First, dried samples (200 mg) were suspended in toluene (30 ml) and APTES (0.19 ml, 0.8 mmol) was added. The mixture was refluxed for 20 h at 110 °C.³¹ Then, amino-modified nanoparticles were obtained by centrifugation at 20000 rpm, washing with ethanol and drying in fume cupboard at 25 °C overnight.

Synthesis of shell particles

Shell nanoparticles with the mean sizes of 28, 54, 98, 135 and 175 nm were also fabricated using Stöber method with the same recipe as the core particle, except for reacting at 70, 60, 50, 40 and 30 °C, respectively. The reactions were first carried out for 20 minutes for the formation of shell particles (28, 54, 98 and 135 nm). For the shell particle of 175 nm, the reaction time is 2 h. In addition, a modified Stöber method was used to fabricate the shell particle of 13 nm diameter.³² First, L-arginine (87 mg) was dissolved in deionized water (69.5 ml) containing octane (5.23 ml). Then, the mixture was sonicated and TEOS (0.5 ml) was added to react at 60 °C for 3.5 h for the formation of shell particles.

Synthesis of RSNs with varied shell sizes

The amino-modified core particle (200 mg) was suspended (2 ml) in DI water (for the synthesis of RSN-211@13) or ethanol (for the synthesis of other RSNs). The core particle suspensions were added into different shell particle reaction solutions as described above (including 69.5 ml of DI water, 87 mg of L-arginine, 5.23 ml of octane and 0.5 ml of TEOS for the synthesis of RSN-211@13; 50 ml of absolute ethanol, 3.8 ml of DI water, 2 ml of ammonium hydroxide solution and 3ml of TEOS for the synthesis of other RSNs), reacting for another 2 h at the original temperatures for shell particle synthesis. The as-synthesized RSNs were washed three times with ethanol and isolated by centrifugation at 4750 rpm for 10 min (shell particles cannot be recovered by centrifugation under these conditions), followed by drying in a fume cupboard at 25 °C overnight. Finally, RSNs were obtained after calcination treatment at 550 °C for 5 h to remove organic components in silica frameworks, enabling all RSNs to have a similar surface composition (amorphous silicon oxide) and surface property (zeta potential).

Hydrophobic modification to RSNs

RSNs were functionalized with n-ODMS. Different RSNs (200 mg) were suspended in toluene (25 ml) containing 0.5% (v/v) n-ODMS. Then, the mixture was refluxed for 20 h at 110 °C, followed by centrifugation at 10000 rpm, washing with ethanol and drying in a fume cupboard at 25 °C overnight.

Characterization

Transmission electron microscopy (TEM) images were taken using a JEOL 1010 microscope operated at 100 kV. The TEM specimens were dispersed in ethanol, and then transferred to a copper grid. The high resolution scanning electron microscopy (HRSEM) images were obtained on a JEOL JSM

7800 FE-SEM equipped with an in-column upper electron detector (UED) and gentle beam technology. HRSEM was operated at a low accelerating voltage of 0.8-1.5 kV with 20% specimen bias.³³ For FE-SEM measurements, the samples were prepared by dispersing the powder samples in DI water, after which they were dropped to the aluminium foil pieces and attached to conductive carbon film on SEM mounts. The SEM mounts were baked in a vacuum oven at 70 °C for at least 8 hours before observations. Dynamic light scattering (DLS) and zeta potential (ZP) measurements were carried out at 25 °C using a Zetasizer Nano-ZS from Malvern Instruments. The samples were dispersed in DI water or ethanol by ultrasonication before analysis. Nitrogen sorption isotherms of the samples were obtained at -196 °C using a Micrometrics Tristar II system. Before the measurements, the samples were degassed at 180 °C overnight in vacuum. The Brunauer–Emmett–Teller specific surface areas (S_{BET}) was calculated using experimental points at a relative pressure of $P/P_0 = 0.05-0.25$. Fourier transform infrared (FTIR) spectra of rough silica nanoparticles before and after hydrophobic modification were collected using the Thermo Scientific™ Nicolet™ 6700 FT-IR spectrometers. Each spectrum was obtained using dried powder against a background measured under the same condition.

Atomic force microscopy (AFM) measurement

IgG-F was mixed with RSN-211@54 (500 µg) in PBS pH 7.4 for 2 h at 4 °C, at a protein concentration of 1 mg ml⁻¹. After incubation, the samples were washed with DI water to remove free and loosely attached proteins and salts in solution by centrifugation and pipetting. Then, the suspension (10 µl) was placed onto silicon wafers. The wafer was evaporated at 25 °C before AFM observation. RSN-211@54 without protein incubation was used as a control. A Cypher S AFM (Asylum Research, an Oxford Instruments company) was used for all the measurements. The images were obtained by employing the tapping mode of the AFM in air by using Al-coated silicon probe with tip radius of 2 nm (NANOSENSORS™, Switzerland).

SPR measurements

The interaction between IgG-F and complementary antigen was monitored utilizing a SPR-based biosensor (Biacore™ T200, GE Healthcare). IgG-F was incubated with RSNs (500 µg) in PBS pH 7.4 for 2 h at 4 °C, and the final protein concentration was 1 mg ml⁻¹. Following that, IgG-F-RSNs complexes were washed several times until the supernatant showed the same UV-vis absorbance at 280 nm as PBS only. Then, IgG-F-RSNs complexes were suspended in HBS-EP buffer (Biacore™ T200, GE Healthcare). Biotinylated peptide was immobilized via streptavidin capture on a sensor chip CAP (GE Healthcare) pre-immobilized with ssDNA-streptavidin (Biotin CAPture kit, GE Healthcare) to yield the peptide surface densities in the range of 2500-5000 R.U. A reference flow cell was generated by omitting only ssDNA-streptavidin onto the chip surface. Interaction analyses were performed by injecting IgG-F-RSNs complexes over the reference and peptide surfaces

in series for 120 seconds at a flow-rate of $10\mu\text{l min}^{-1}$. Complex dissociation was monitored for 120 seconds. The binding intensity was determined at the peak point 128 seconds after sample injection. Surface regeneration was performed at the end of each analysis cycle by injecting guanidine (8 M) mixed with NaOH (1 M) at the ratio of 3:1, followed by washing with the mixture of acetonitrile (30%), NaOH (0.25 M) and SDS (0.05%).

Protein adsorption assay

The adsorption ability of RSNs with different proteins (cytochrome *c*, IgG-F and IgG-A) was evaluated. Different proteins were mixed with RSNs (100 μg) in PBS pH 7.4 for 2 h at 4 °C, and final protein concentration is 1 mg ml^{-1} . IgG-A was also incubated with C18-RSNs. After this time, the mixtures were centrifuged at 15000 rpm, and the supernatants were collected for testing. The adsorption of protein molecules was determined using a NANODROP 1000 spectrophotometer (Thermo Scientific) at 280 nm.

Protein therapeutics assay

Cells were maintained as monolayer cultures at 37 °C and 5% CO_2 in DMEM supplemented with 10% FBS and 1% penicillin-streptomycin. MCF-7 cells were seeded in 24 well-plates at 5×10^4 cells per well and incubated for 4~6 h. The dose-dependent cytotoxicity of C18-RSN-211@98+anti-pAkt composite was tested. The anti-pAkt antibody (1 mg ml^{-1} , sigma) was incubated with C18-RSN-211@98 in PBS pH 7.4 at 4 °C for 2 h. Following this, protein-nanoparticle complexes were suspended in serum containing culture medium in two-fold dilutions. The highest nanoparticle concentration is 50 $\mu\text{g ml}^{-1}$, corresponding to 1 $\mu\text{g ml}^{-1}$ of anti-pAkt antibody on the surface of the nanoparticle. Non-specific rabbit IgG-A and nanoparticle only were used as control. After incubation for 24 h, cells were detached by incubating with trypsin/EDTA mixture. Detached cells were then suspended in the medium previously collected from the sample. Cell suspension was diluted with trypan blue solution in a 1:1 ratio, and live and dead cells were counted on a hemacytometer.

The comparison of protein therapeutics among all the C18-RSNs was also evaluated. The same amount of C18-RSNs (50 μg) was mixed with anti-pAkt antibody (1 μg) in PBS pH 7.4 at 4 °C for 2 h and the complexes were incubated with MCF-7 cells in serum containing culture medium for 24 h at the nanoparticle concentration of 15 $\mu\text{g ml}^{-1}$. Non-specific rabbit IgG-A and C18-RSNs only were used as control. The cell viability was also determined by counting live and dead cells.

Detection of cellular uptake performance of C18-RSNs

To quantitatively compare cellular uptake performance of C18-RSNs, 3×10^5 MCF-7 cells were seeded in 6-well plates one day before transfection. C18-RSNs (50 $\mu\text{g ml}^{-1}$) were incubated with cells under serum free condition for 4 h. Afterwards, the cells were washed with PBS three times and harvested with trypsin. Cell number for each sample was recorded. After centrifugation, the cell pellets were washed twice and dried. DI

water was added to allow dissolution of the cells under ultrasonication condition. The supernatants (containing cell components) were removed by centrifugation at 15000 rpm for 5 min. Aqueous NaOH solution (1 M) was then added to allow dissolution of silica nanoparticles with ultrasound. The silicon concentrations in the final solutions were measured by inductively coupled plasma optical emission spectrometry (ICPOES) using a Vista-PRO instrument (Varian Inc, Australia), which were then converted to be the mass of silica per cell.

Western-blot analysis

MCF-7 cells were seeded in 6-well plates at a seeding density of 3×10^5 cells per well. The anti-pAkt antibody and the non-specific IgG-A were incubated with C18-RSN-211@98 in PBS pH 7.4 at 4 °C for 2 h. Then, protein-nanoparticle complexes, along with C18-RSN-211@98 only group, were mixed with serum containing culture medium and incubated with cells for 24 h. The final concentration of nanoparticles is 50 $\mu\text{g ml}^{-1}$ and protein is 1 $\mu\text{g ml}^{-1}$. At the end of incubation, cells were washed with PBS and lysed. The solutions containing cell lysates were denatured at 95 °C for 15 min followed by characterization by SDS-PAGE. The protein bands were transferred to a PVDF membrane. Bcl-2 bands were targeted using Bcl-2 monoclonal antibody (mAb) as the primary antibody, and HRP-linked anti-rabbit IgG antibody as the secondary antibody. GAPDH mAb was used as an internal reference. Bands were visualized on a ChemiDoc MP System (Bio-Rad).

Results and Discussion

Preparation of RSNs

Three relatively large silica shell particles (28 \pm 3 nm, Figure S1b, ZP -42 \pm 8.3 mV; 54 \pm 5 nm, Figure S1c, ZP -53 \pm 2.6 mV; 98 \pm 7 nm, Figure S1d, ZP -53 \pm 1.0 mV) were prepared by the classical Stöber method.³⁰ The smallest silica shell particle (13 \pm 2 nm, Figure S1a, ZP -42 \pm 2.4 mV) was synthesized by a modified Stöber method.³² The silica core particle (diameter of 211 \pm 11 nm, Figure S1g, ZP +31 \pm 0.2 mV) was also fabricated using the classical Stöber method, followed by amino-modification to generate positive charges on the surface. The particle size distribution curves measured by the DLS method are narrow for all silica particles (Figure S1h), indicating that the nanoparticles are monodispersed and uniform in size (see Table S1 for the polydispersity index, PDI).

To fabricate RSNs with varied shell sizes, the core particles were suspended and added into the reaction solution of different shell particles. After reaction for 2 h and washing, the final calcined samples were denoted as RSN-211@13, RSN-211@28, RSN-211@54 and RSN-211@98, possessing ZP values of -30, -26, -29 and -29 mV, respectively. The numbers before and after @ refer to the mean size of core particle and shell particles measured from TEM images (Figure S1). The core-to-shell size is 16.2:1, 7.5:1, 3.9:1 and 2.2:1, respectively.

TEM images of four RSNs are shown in Fig. 1. The particle size of RSN-211@13, RSN-211@28, RSN-211@54 and RSN-211@98

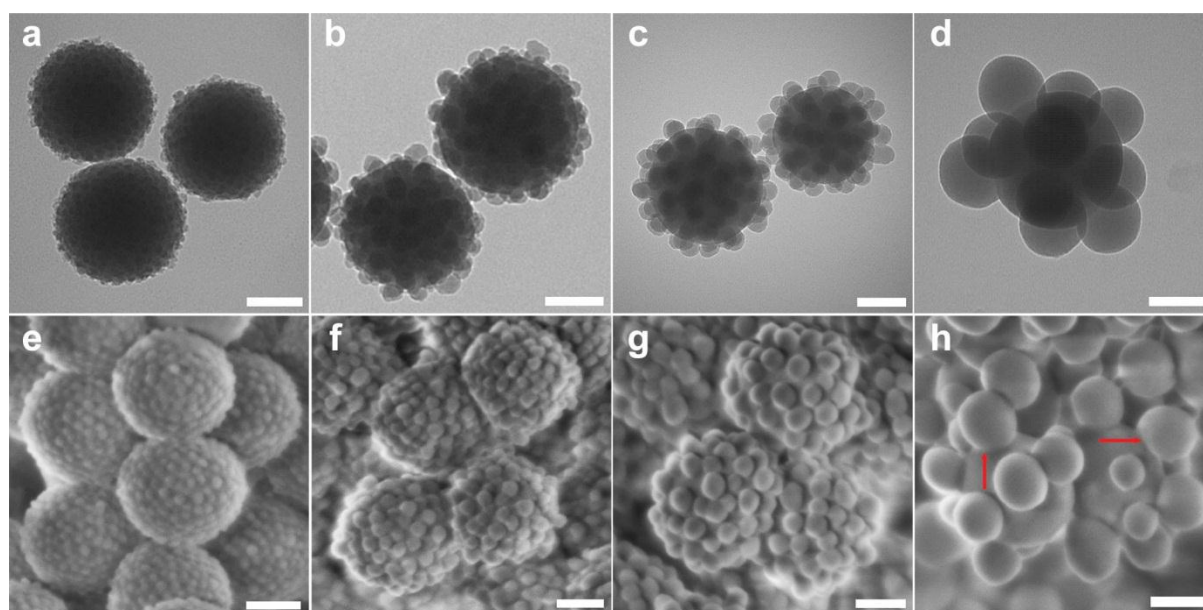


Fig. 2 TEM (a-d) and HRSEM (e-h) images of RSNs with varied shell particle sizes: a&e) RSN-211@13, b&f) RSN-211@28, c&g) RSN-211@54, d&h) RSN-211@98 and the red arrows indicate the formation of bigger “necks” connecting shell and core particles. Scale bar: 100nm.

is 254 ± 26 , 270 ± 15 , 297 ± 20 and 380 ± 39 nm, respectively (Fig. 2a-d). HRSEM images (Fig. 2e-h) clearly show that core particles are uniformly studded by different shell particles, and the interspace size between neighbouring shell particles enlarges as the shell particle size increase from ~ 13 to ~ 98 nm. The interspace size between shell particles is crucial to the accumulation of cargo molecules. Although the interspace sizes for RSNs are not uniform and difficult to measure precisely, the values were determined by measuring 50 edge-to-edge interspacing between adjacent shell particles to allow a semi-quantitative comparison. As shown in Figure S2 and Table S2, the average interspace size of RSN-211@13, RSN-211@28, RSN-211@54 and RSN-211@98 is 7 ± 2 , 14 ± 4 , 21 ± 9 and 38 ± 22 nm, respectively. The particle sizes of the four samples from DLS measurements are close to that obtained from TEM measurements and the small PDI values confirm that all RSNs are uniform and well-dispersed (Table S2).

The nitrogen sorption analysis was further utilized to measure S_{BET} of RSN-211@13, RSN-211@28, RSN-211@54 and RSN-211@98, which is 25.4 , 26.9 , 25.2 and 22.4 $\text{m}^2 \text{g}^{-1}$, respectively (Table S2). For RSN-211@28, RSN-211@54 and RSN-211@98 prepared by the same protocol, S_{BET} of RSNs decrease with increasing shell particle size. The lower S_{BET} of RSN-211@13, compared to that of RSN-211@28, can be attributed to the difference in synthesis methods: a longer reaction time (3.5 h vs. 20 min) of shell particles may lead to more condensed structures and thus reduced surface area.

Using our previous protocol,²¹ shell particles of ~ 13 nm were successfully attached on the core particles of 211 nm. However, larger shell particles, for example, with the size of ~ 28 nm, are easily peeled off from core particles during

washing and drying processes (Figure S3a), even the core-shell structures were formed in solution (Figure S3b). In the current approach, the large shell particles (~ 28 , ~ 54 and ~ 98 nm) were formed using the classical Stöber method after reaction of 20 min, as the particle sizes were barely changed after about 15 min.³⁰ Afterwards, positively charged core particle suspension was added into the above shell particle reaction solution. By comparing the difference of current synthesis strategy to the previous one (shown in Fig. 1), the pH value of reaction medium (11.0 vs. 9.4) and the weight ratio of shell to core particles (4:1 vs. <1:1) is increased (Fig. 1a(i) vs. b(i)).

The driving force for the attachment of negatively charged shell particles onto positively charged core particles is electrostatic interaction^{21, 22} (Fig. 1a(ii) and 1b(ii)), however less attention has been paid to how to stabilize the formed core-shell structure and hence it is difficult to synthesize rough particles with relatively large shell sizes. The focus of this study is to address this challenge through silicate chemistry.³⁴ At pH 9.4 the silica solubility is reduced with both $\text{SiO}(\text{OH})_3^-$ ($\sim 50\%$) and $\text{Si}(\text{OH})_4$ ($\sim 50\%$) presenting in solution (Scheme 2b(i)). In contrast, at a stronger basic condition of pH 11, $\text{SiO}(\text{OH})_3^-$ is the predominant silicate species with a relatively high concentration and thus more negative charges (Fig. 1a(i)). When shell particles attach to core particles, a space with surfaces of negative curvature is generated as indicated by a violet arrow in Fig. 1a(ii). The solubility of a surface with negative curvature is lower than that with positive curvature (i.e., normal surface of spheres). Therefore, the net result is silica migration and deposition into the space near the point of contact between core and shell particles,³⁵ leading to the

formation of a bigger "neck" connecting core and shell particles (indicated by a violet arrow in Fig. 1a(iii)).

The solubility difference between surfaces with positive and negative curvatures increases with pH (e.g., 11.0 vs. 9.4), thus a higher pH favours the formation of bigger "necks"³⁵ stabilizing the rough particle morphology. If the neck size is small and not strong enough (e.g., at pH of 9.4) to hold core and shell particles (especially shell particles with relatively larger sizes), the shell particles adhered on core particle surface mainly through electrostatic interaction would easily peel off (iii in Fig. 1b) during the subsequent treatments (washing, drying, sonication, etc.). In addition to the increase of pH, the shell particle concentration is also increased in our synthesis, which is beneficial for the attachment between core and shell particles and eventually the enhanced neck formation.

The "neck-enhancing" mechanism for core-shell connection is supported by experimental observations. The formation of neck regions between shell and core particles can be directly seen using RSN-211@98 as an example (indicated by red arrows in Fig. 2h). Noticeably, there is a limitation for our current method. When the shell size was further increased to 135 nm (Figure S1e, 135±8nm, ZP -33±1.9 mV) and 175nm (Figure S1f, 175±8nm, ZP -32±0.9 mV), the even larger shell particles failed to attach on the surface of core particles (Figure S4).

Protein adsorption behaviours on RSNs

To investigate the influence of interspace size of RSNs on protein adsorption capacity, three model proteins with various molecular weights, including cytochrome c, IgG-F and a non-specific rabbit IgG-A were used. Non-specific rabbit IgG-A was chosen because it has a similar structure and animal source with anti-pAkt antibody, which will be utilized as the therapeutic protein in the following biological study. Among the three proteins, cytochrome c has an isoelectric point (IEP) of ~10, a diameter of ~3 nm and the smallest molecular weight of ~12 kDa.³⁶ IgG-A with the largest molecular weight of 150 kDa has a diameter of ~20 nm¹⁹ and the IEP of ~9. The IgG-F is a domain antibody and exists as a dimer, which has an IEP value of ~8 and a molecular weight of 76 kDa with an estimated diameter of 10 nm. All proteins can be directly loaded onto RSNs at pH 7.4 in a phosphate buffer solution (PBS) due to the electrostatic interaction between negatively charged silica nanoparticles (Figure S5) and the positively charged proteins. All RSNs demonstrate higher adsorption ability in three tested proteins compared to the smooth core particles (data not shown), which is consistent with previously reported results.²¹

Fig. 2 shows protein adsorption capacity of RSNs with various interspace sizes. RSN-211@98 with the interspace size of ~38 nm exhibits the highest adsorption ability (22.6 $\mu\text{g mg}^{-1}$) of IgG-A. RSN-211@54 (18.1 $\mu\text{g mg}^{-1}$) and RSN-211@28 (17.2 $\mu\text{g mg}^{-1}$) with small interspace sizes show lower adsorption amount. In addition, the IgG-A adsorption ability of RSN-211@98 is ~78% higher than RSN-211@13 (12.7 $\mu\text{g mg}^{-1}$),

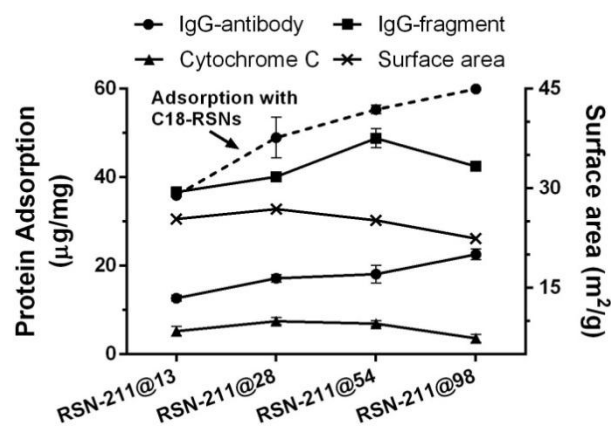


Fig. 3 Protein Adsorption profiles (● IgG-A; ■ IgG-F; ▲ cytochrome c). Solid lines represent different protein adsorption onto unmodified rough silica nanoparticles. The dash line also represents the IgG-A adsorption onto different rough silica nanoparticles, except they are all modified with C18-groups. Data represent mean \pm SD. Specific surface area variations (×) of different unmodified rough silica nanoparticles are displayed to compare with protein adsorption trend.

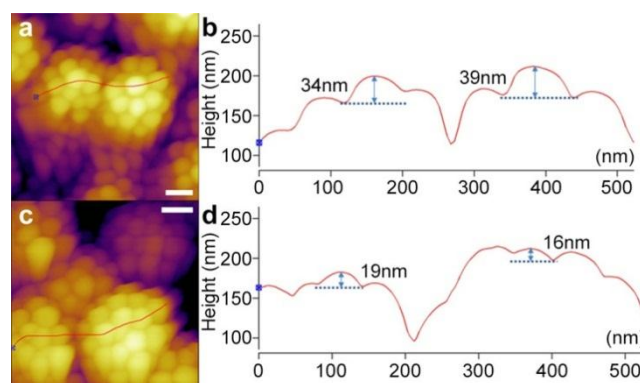


Fig. 4 Surface topography studies. AFM images of RSN-211@54 before (a) and after (c) the adsorption of IgG-F. A cross-sectional line is drawn to characterize the height changes of shell particles on the top region before (b) and after (d) protein adsorption. Scale bar: 100 nm.

which has the smallest interspace size. For IgG-F, the adsorption behaviour becomes different. RSN-211@54 exhibits the highest protein entrapment ability (48.8 $\mu\text{g mg}^{-1}$). RSN-211@98 shows a lower loading capacity of 42.5 $\mu\text{g mg}^{-1}$, because the interspace size of RSN-211@98 is too large to hold the relatively small protein molecules in the voids.¹⁷ The lower adsorption ability of RSN-211@28 (40.1 $\mu\text{g mg}^{-1}$) and RSN-211@13 (36.7 $\mu\text{g mg}^{-1}$) is attributed to the smaller void size compared to RSN-211@54.

Noticeably, adsorption trend depends on the void size but not the surface area of RSNs (Fig. 3, solid line with cross symbol). As calculated in Table S3, the protein coverage (adsorption capacity versus surface area) is 63%, 80%, 91% and 127% for IgG-A, 91%, 94%, 122% and 117% for IgG-F on RSN-211@13,

RSN-211@28, RSN-211@54 and RSN-211@98, respectively. The multilayer deposition behaviour of IgG-A on RSN-211@98 and IgG-F on both RSN-211@54 and RSN-211@98 suggests that the adsorption occurs in the interspace of particles with rationally controlled surface roughness.³⁷

To confirm this hypothesis, RSN-211@54 was chosen to explore the surface topography changes before and after IgG-F adsorption using AFM, due to its highest protein adsorption capacity among the three cases. As shown in Fig. 3, at the top region, shell particle height of pure RSN-211@54 (Fig. 4a, b) is 34–39 nm. After IgG-F adsorption, the shell particle height (Fig. 4c, d) decreases to 16–19 nm, suggesting that protein molecules are entrapped and accumulated into the shell interspaces of RSN-211@54.

When protein size is much smaller than the interspace size, the surface area change dominates protein adsorption behaviour. For the adsorption of cytochrome *c*, RSN-211@28 ($7.5 \mu\text{g mg}^{-1}$) shows the highest adsorption ability, followed by RSN-211@54 ($6.9 \mu\text{g mg}^{-1}$). The adsorption ability of RSN-211@13 and RSN-211@98 are only 5.2 and $3.6 \mu\text{g mg}^{-1}$, respectively. This adsorption trend is consistent with S_{BET} variations (Fig. 3, solid line with cross symbol) of different RSNs. In addition, the coverage is calculated to be at most 9% (RSN-211@28, Table S3). These results demonstrate that the interspace sizes of RSNs are too large to confine very small protein molecules.

Desired surface functionality (e.g., octadecyl-group¹⁶) is of significance for high loading and efficient delivery of therapeutic proteins into cells. All RSNs were hydrophobically-modified on the surface, referred to as C18-RSN-211@13, C18-RSN-211@28, C18-RSN-211@54 and C18-RSN-211@98 with slightly increased ZP values of -23 , -18 , -25 and -25 mV, respectively. They are used to further investigate the interspace size influence of C18-RSNs on IgG-A adsorption capacity for the following application in therapeutic protein delivery. FTIR results confirm the successful conjugation of octadecyl-groups for all C18-RSNs (Figure. S5). No significant topography changes are observed under TEM images for all samples (Figure. S6).

The IgG-A adsorption ability of C18-RSNs is displayed in Fig. 3 (dash line). C18-RSNs show highly improved adsorption capacity, compared to unmodified RSNs. The protein coverage is calculated to be 179% for C18-RSN-211@13 ($37 \mu\text{g mg}^{-1}$), 229% for C18-RSN-211@28 ($49 \mu\text{g mg}^{-1}$), 277% for C18-RSN-211@54 ($55 \mu\text{g mg}^{-1}$) and 337% for C18-RSN-211@98 ($60 \mu\text{g mg}^{-1}$). The results are interpreted as IgG-A adsorption in a multi-layered fashion, both on surface and in voids, where some proteins did not necessarily have strongly physical contact with the silica surface.¹⁹ In addition, the adsorption amount of IgG-A to C18-RSNs is much higher than the results in literature,¹⁶ where IgG-A loading capacity of octadecyl-group modified smooth solid silica nanoparticles is only $1.25 \mu\text{g mg}^{-1}$.

The surface chemistry and nanoscale roughness play important roles in the immobilization of biomolecules. The adsorption of positively charged IgG-A in PBS onto negatively charged RSNs is mainly attributed to the electrostatic attraction.³⁸ For C18-RSNs, the hydrophobic modification leads to partially reduced

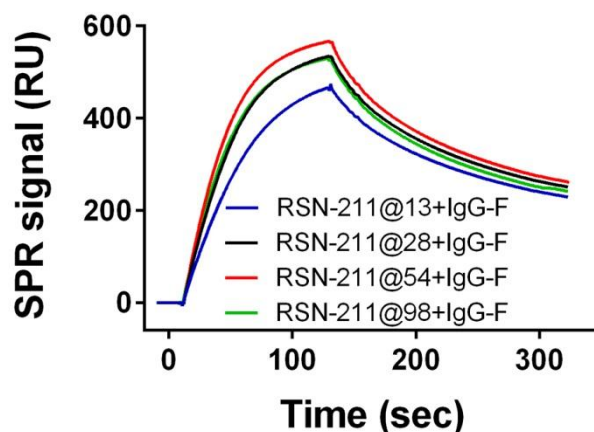


Fig. 5 SPR sensorgrams showing the binding signals of RSN-IgG-F complexes with receptors. All RSN-IgG-F complexes showed positive values of the binding with ligand.

charge density compared to corresponding RSNs, however the IgG-A adsorption capacity was increased as much as 2–3 times than that of RSNs. For example, C18-RSN-@211@13 shows 2.8 times of IgG antibody adsorption compared to RSN-211@13 without C18 modification (Fig. 3), indicating that the hydrophobic interaction is more important than the electrostatic interaction in this case.^{38,39} However, when comparing the adsorption capacity of either RSNs or C18-RSNs with the same surface chemistry but tunable surface roughness (Fig. 3), it shows that the size of surface voids (or core-to-shell ratios) is also important, e.g. the IgG-A adsorption capacity of C18-RSN-@211@98 is 1.7 times compared to C18-RSN-@211@13, which is attributed to protein immobilization in the void spaces of rough surfaces.³⁷

Evaluation on protein binding ability

Protein secondary structures are possibly disturbed after absorbed onto nanoparticle surface.⁴⁰ It is very important to maintain the activity of protein molecules loaded into nano-carriers for therapeutic applications. Therefore, SPR measurements were conducted to evaluate whether the binding capability of IgG-F with its complementary antigen will be maintained after contacting rough nanoparticles.

SPR is a fast and real-time detection technique used to examine the interaction between wide ranges of biological targets. Based on detecting small changes in the refractive index, SPR is able to specifically monitor the interaction between analytes (e.g., antibody or peptide) and the ligand molecules (e.g., antigen), which have been immobilized onto an inert surface. "Resonance units" (RU, equal to a critical angle shift of 10^{-4} deg) is used to describe binding signals between analytes and ligands.⁴¹ Unmodified RSNs were used to absorb IgG-F in this test, because IgG-F is immobilized on unmodified RSNs generally in a monolayer manner, so that the SPR results can be directly compared with the protein binding ability. After sample injection, the negative signals from the control groups demonstrate that bare RSNs and PBS did not

exhibit any binding events. In comparison, all RSN-IgG-F complexes show positive signals in binding with the antigen, which has been immobilized to the sensor chip as the ligand, indicating the binding activity of IgG-F is maintained after complexing with all RSNs (Fig. 4 and Table S4). It is noted that the trend of SPR signal intensity (peaked at 128 seconds after sample injection) of various RSNs-IgG-F complexes is consistent with the adsorption trend of IgG-F onto various RSNs (Fig. 3).

Typically, there is a linear relationship between the SPR signal intensity and the surface concentration of immobilized molecules.⁴¹ In our test, equal amount of RSNs was mixed with excessive amount of IgG-F in PBS solution to achieve a saturated adsorption of IgG-F on complexes. After removing free IgG-F and re-suspending into the injection buffer, the SPR test for each sample is generally finished after 10 min of re-suspending the IgG-F/RSNs complexes to ensure a minimized release of IgG-F from RSNs.⁴² The IgG-F coverage of RSN-211@54 is 122%; however, RSN-211@13 and RSN-211@28 with relatively low IgG-F adsorption are not fully covered. Therefore, higher IgG-F density on the surface of RSNs favours the binding with ligands on the sensor chip⁴³ and generates higher SPR signal intensity. As a result, RSN-211@54 shows the highest SPR signal intensity followed by RSN-211@28, and RSN-211@13 has the lowest SPR signal intensity. Besides the influence of protein coverage on particle surface, higher shell particle density provides more voids for accommodating IgG-F. RSN-211@98 with the largest shell particle size and thus the lowest void density on the surface has less binding sites with ligands, leading to an even lower SPR intensity, compared to RSN-211@28.

Intracellular delivery of therapeutic protein

It has been reported that pAkt plays an important role in transcriptional activation of proteins involved in cell growth.⁴⁴ Delivering anti-pAkt antibody into cytosols inactivates pAkt and induces the decrease of anti-apoptotic protein (e.g. Bcl-2⁴⁵), resulting in apoptosis in some human cancer cell lines, for example, ovarian cancer, breast cancer and pancreatic cancer.⁴⁶⁻⁴⁸ Hydrophobic-modified silica nanoparticles have been reported to deliver therapeutic proteins successfully into cytoplasm.^{16, 17} In this study, C18-RSN-211@98 was used to deliver anti-pAkt antibody (Fig. 1c) into human breast cancer cells (MCF-7) due to its highest antibody adsorption ability. Dose-dependent cell inhibition is observed for the complex of C18-RSN-211@98+anti-pAkt, and a maximum exposure of $1 \mu\text{g ml}^{-1}$ of immobilized anti-pAkt antibody at $50 \mu\text{g ml}^{-1}$ of nanoparticle shows an increase in cell inhibition up to 85% (Fig. 6a). This cell inhibition of anti-pAkt antibody is greater than the literature report, where ~80% of cell inhibition was induced by using as high as $800 \mu\text{g ml}^{-1}$ of a C18-modified silica nanoparticle (15 nm in diameter) to deliver $1 \mu\text{g}$ of anti-pAkt antibody. In the absence of silica nano-carrier, free anti-pAkt antibody is unable to cause cell inhibition, indicating its poor cell internalization ability (Figure S7). In addition, when cells were treated with C18-RSN-211@98+non-specific rabbit IgG-A

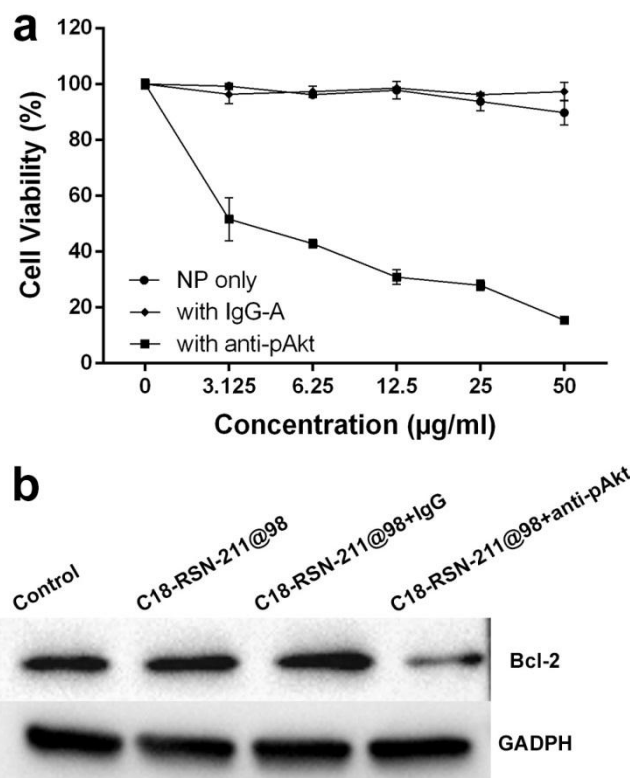


Fig. 6 Cell inhibition by the delivery of therapeutic protein. a) Cell viability of MCF-7 cells incubated with increasing concentrations of C18-RSN-211@98+anti-pAkt (■), C18-RSN-211@98+non-specific-IgG-A (◆) and C18-RSN-211@98. Data represent mean \pm SD. b) Western blotting confirming the degradation of downstream anti-apoptotic protein, Bcl-2 in MCF-7 cells. Blots presented are representative of typical results. GAPDH is served as an internal reference.

or nanoparticle only, no obvious cell inhibition is observed (Fig. 6a). The anti-pAkt antibody delivery efficiency was also evaluated using other C18-RSNs (as shown in Figure S8), and C18-RSN-211@98 holds the best performance.

To further test the downstream effects after blocking pAkt, Bcl-2 degradation was evaluated using western blotting. As shown in Fig. 6b, Bcl-2 degradation in MCF-7 cells is only observed following cytosolic delivery of the C18-RSN-211@98+anti-pAkt, compared to cell only, nanoparticle only and nanoparticle with non-specific IgG-A groups, indicating that cell inhibition is associated with the degradation of Bcl-2 levels in MCF-7 cells.

Conclusions

In summary, rough silica nanoparticles (RSNs) with varied topographies were successfully synthesized using a novel "neck-enhancing" approach. Relatively high pH value and shell particle concentration favour the formation of bigger "necks", which is crucial for the generation of RSNs with controllable core-to-shell ratios. The increase of shell particle sizes from ~13 to ~98 nm while keeping the core particle size

at ~211 nm enlarges the shell particle interspace size from ~7 to ~38 nm, where proteins with comparable sizes are favourably accumulated without influencing its binding ability. The rough silica nanoparticles with an optimized loading capacity demonstrate a high efficiency of intracellular delivery of therapeutic proteins in cancer cells, causing a significant cell inhibition. The "neck-enhancing" approach provides new understanding in the rational design of cellular delivery vectors with controllable surface roughness for the delivery of therapeutic proteins.

Acknowledgements

The authors acknowledge the Australian Research Council for financial support. We are grateful for use of the facilities, and the scientific and technical assistance, of the Australian National Fabrication Facility and the Australian Microscopy and Microanalysis Research Facility at the Centre for Microscopy and Microanalysis, The University of Queensland. Author 1 and Author 2 contributed equally to this work.

Notes and references

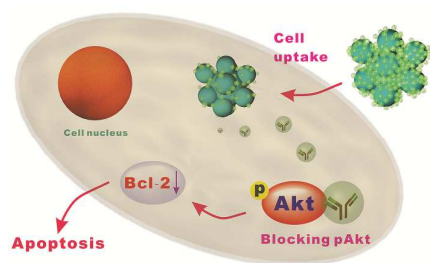
- B. Leader, Q. J. Baca and D. E. Golan, *Nat. Rev. Drug. Discov.*, 2008, **7**, 21-39.
- M. Yan, J. J. Du, Z. Gu, M. Liang, Y. F. Hu, W. J. Zhang, S. Priceman, L. L. Wu, Z. H. Zhou, Z. Liu, T. Segura, Y. Tang and Y. F. Lu, *Nat. Nanotechnol.*, 2010, **5**, 48-53.
- S. Frokjaer and D. E. Otzen, *Nat. Rev. Drug. Discov.*, 2005, **4**, 298-306.
- A. Sood and R. Panchagnula, *Chem. Rev.*, 2001, **101**, 3275-3303.
- F. Cuomo, A. Ceglie and F. Lopez, *J. Colloid Interface Sci.*, 2012, **365**, 184-190.
- H. Kamiya, Y. Fujimura, I. Matsuoka and H. Harashima, *Biochem. Biophys. Res. Commun.*, 2002, **298**, 591-597.
- X. Zhou and L. Huang, *J. Controlled Release*, 1992, **19**, 269-274.
- Z. J. Wang, L. Qian, X. L. Wang, F. Yang and X. R. Yang, *Colloid Surface A*, 2008, **326**, 29-36.
- I. Moret, J. Esteban Peris, V. M. Guillem, M. Benet, F. Revert, F. Dasí, A. Crespo and S. F. Aliño, *J. Controlled Release*, 2001, **76**, 169-181.
- G. Navarro and C. Tros de Ilarduya, *Nanomed. Nanotechnol. Biol. Med.*, 2009, **5**, 287-297.
- X.-B. Xiong, H. Uludağ and A. Lavasanifar, *Biomaterials*, 2009, **30**, 242-253.
- G. Maiorano, S. Sabella, B. Sorce, V. Brunetti, M. A. Malvindi, R. Cingolani and P. P. Pompa, *ACS Nano*, 2010, **4**, 7481-7491.
- F. Osaki, T. Kanamori, S. Sando, T. Sera and Y. Aoyama, *J. Am. Chem. Soc.*, 2004, **126**, 6520-6521.
- Y. Zhu, W. Meng, H. Gao and N. Hanagata, *J. Phys. Chem. C*, 2011, **115**, 13630-13636.
- S. F. Ye, M. M. Tian, T. X. Wang, L. Ren, D. Wang, L. H. Shen and T. Shang, *Nanomed-Nanotechnol.*, 2012, **8**, 833-841.
- S. S. Bale, S. J. Kwon, D. A. Shah, A. Banerjee, J. S. Dordick and R. S. Kane, *ACS Nano*, 2010, **4**, 1493-1500.
- J. Zhang, S. Karmakar, M. H. Yu, N. Mitter, J. Zou and C. Z. Yu, *Small*, 2014, **10**, 5068-5076.
- I. I. Slowing and V. S. Y. Lin, *J. Am. Chem. Soc.*, 2007, **233**, 186-186.
- M. Holmberg and X. Hou, *Langmuir*, 2009, **25**, 2081-2089.
- K. Grunewald, P. Desai, D. C. Winkler, J. B. Heymann, D. M. Belnap, W. Baumeister and A. C. Steven, *Science*, 2003, **302**, 1396-1398.
- Y. T. Niu, M. H. Yu, S. B. Hartono, J. Yang, H. Y. Xu, H. W. Zhang, J. Zhang, J. Zou, A. Dexter, W. Y. Gu and C. Z. Yu, *Adv. Mater.*, 2013, **25**, 6233-6237.
- G. L. Li, X. L. Yang and J. Y. Wang, *Colloid Surface A*, 2008, **322**, 192-198.
- C. S. Wagner, S. Shehata, K. Henzler, J. Yuan and A. Wittemann, *J. Colloid Interf Sci.*, 2011, **355**, 115-123.
- B. Zhao and M. M. Collinson, *Chem. Mater.*, 2010, **22**, 4312-4319.
- F. Lu, S. H. Wu, Y. Hung and C. Y. Mou, *Small*, 2009, **5**, 1408-1413.
- Y. Niu, A. Papat, M. Yu, S. Karmakar, W. Gu and C. Yu, *Ther. Deliv.*, 2012, **3**, 1217-1237.
- Z. Yuhong, Z. Qichao, S. Xingwang, T. Qingqiong, C. Min and W. Limin, *J. Colloid Interf Sci.*, 2009, **336**, 544-550.
- M. W. Pi, T. T. Yang, J. J. Yuan, S. Fujii, Y. Kakigi, Y. Nakamura and S. Y. A. Cheng, *Colloid Surface B*, 2010, **78**, 193-199.
- H. S. Hwang, S. B. Lee and I. Park, *Mater. Lett.*, 2010, **64**, 2159-2162.
- W. Stober, A. Fink and E. Bohn, *J. Colloid Interface Sci.*, 1968, **26**, 62-69.
- P. Shah, N. Sridevi, A. Prabhune and V. Ramaswamy, *Micropor. Mesopor. Mat.*, 2008, **116**, 157-165.
- T. Yokoi, Y. Sakamoto, O. Terasaki, Y. Kubota, T. Okubo and T. Tatsumi, *J. Am. Chem. Soc.*, 2006, **128**, 13664-13665.
- S. Asahina, S. Uno, M. Suga, S. M. Stevens, M. Klingstedt, Y. Okano, M. Kudo, F. Schüth, M. W. Anderson, T. Adschiri and O. Terasaki, *Micropor. Mesopor. Mat.*, 2011, **146**, 11-17.
- C. J. Brinker and G. W. Scherer, in *Sol-Gel Science*, eds. C. J. Brinker and G. W. Scherer, Academic Press, San Diego, USA, 1990, pp. 96-233.
- R. K. Iler, *The chemistry of silica: Solubility, polymerization, colloid and surface properties, and biochemistry*, A Wiley-Interscience Publication, New York, USA, 1979.
- I. I. Slowing, B. G. Trewyn and V. S. Y. Lin, *J. Am. Chem. Soc.*, 2007, **129**, 8845-8849.
- P. E. Scopelliti, A. Borgonovo, M. Indrieri, L. Giorgetti, G. Bongiorno, R. Carbone, A. Podesta and P. Milani, *Plos One*, 2010, **5**, e11862.
- W. Norde, *Macromol Symp.*, 1996, **103**, 5-18.
- M. Holmberg and X. L. Hou, *Langmuir*, 2009, **25**, 2081-2089.
- P. Roach, D. Farrar and C. C. Perry, *J. Am. Chem. Soc.*, 2006, **128**, 3939-3945.
- M. Besenicar, P. Macek, J. H. Lakey and G. Anderluh, *Chem. Phys. Lipids*, 2006, **141**, 169-178.

Paper

Journal Name

- 42 C. H. Lei, P. Liu, B. W. Chen, Y. M. Mao, H. Engelmann, Y. Shin, J. Jaffar, I. Hellstrom, J. Liu and K. E. Hellstrom, *J. Am. Chem. Soc.*, 2010, **132**, 6906–6907.
- 43 M. Canovi, J. Lucchetti, M. Stravalaci, F. Re, D. Moscatelli, P. Bigini, M. Salmona and M. Gobbi, *Sensors-Basel*, 2012, **12**, 16420-16432.
- 44 J. J. Wallin, J. Guan, W. W. Prior, K. A. Edgar, R. Kassees, D. Sampath, M. Belvin and L. S. Friedman, *Sci. Transl. Med.*, 2010, **2**, 48ra66.
- 45 S. C. Tsai, C. C. Lu, C. Y. Lee, Y. C. Lin, J. G. Chung, S. C. Kuo, S. Amagaya, F. N. Chen, M. Y. Chen, S. F. Chan and J. S. Yang, *Int. J. Oncol.*, 2012, **41**, 1683-1692.
- 46 N. Itoh, S. Semba, M. Ito, H. Takeda, S. Kawata and M. Yamakawa, *Cancer*, 2002, **94**, 3127-3134.
- 47 O. David, J. Jett, H. LeBeau, G. Dy, J. Hughes, M. Friedman and A. R. Brody, *Clin. Cancer. Res.*, 2004, **10**, 6865-6871.
- 48 O. Stal, G. Perez-Tenorio, L. Akerberg, B. Olsson, B. Nordenskjold, L. Skoog and L. E. Rutqvist, *Breast. Cancer. Res.*, 2003, **5**, R37-R44.

Table of content entry



Silica nanoparticles with controllable surface roughness have been successfully prepared for therapeutic anti-pAkt antibody delivery.